Journal of
Synchrotron
Radiation

ISSN 0909-0495

Received 28 March 2012
Accepted 30 September 2012

IR and X-ray time-resolved simultaneous experiments: an opportunity to investigate the dynamics of complex systems and non-equilibrium phenomena using third-generation synchrotron radiation sources

Augusto Marcelli,[a]* Plinio Innocenzi,[b] Luca Malfatti,[b] Mark A. Newton,[c] Julietta V. Rau,[d] Eglof Ritter,[e] Ulrich Schade[f] and Wei Xu[g]

[a]INFN, Laboratori Nazionali di Frascati, Via E. Fermi 40, 00044 Frascati, Rome, Italy, [b]Laboratorio di Scienza dei Materiali e Nanotecnologie LMNT, Università di Sassari, CR-INSTM, CNBS, Palazzo Pou Salit, Piazza Duomo 6, 07041 Alghero, Sassari, Italy, [c]ESRF, 6 rue Jules Horowitz, BP 220, F-38043 Grenoble, France, [d]Istituto di Struttura della Materia, CNR, Via del Fosso del Cavaliere 100, 00133 Rome, Italy, [e]Charité, Universitätsmedizin Berlin, Institut für Medizinische Physik und Biophysik, Ziegelstrasse 5-9, 10117 Berlin, Germany, [f]Helmholtz-Zentrum Berlin für Materialien und Energie GmbH, Elektronenspeicherring BESSY II, Albert-Einstein-Strasse 15, D-12489 Berlin, Germany, and [g]Institute of High Energy Physics, Chinese Academy of Science, Beijing 100049, People's Republic of China. E-mail: marcelli@lnf.infn.it

Third-generation storage rings are modern facilities working with high currents and designed to host powerful radiation sources, like undulators and wigglers, and to deliver high-brilliance beams to users. Many experiments at high spatial resolution, such as spectromicroscopy at the nanometre scale and with high temporal resolution to investigate kinetics down to the picosecond regime, are now possible. The next frontier is certainly the combination of different methods in a unique set-up with the ultimate available spatial and temporal resolutions. In the last decade much synchrotron-based research has exploited the advantage of complementary information provided by time-resolved X-ray techniques and optical methods in the UV/Vis and IR domains. New time-resolved and concurrent approaches are necessary to characterize complex systems where physical–chemical phenomena occur under the same experimental conditions, for example to detect kinetic intermediates *via* complementary but independent observations. In this contribution we present scientific cases from original works and literature reviews to support the proposed IR/X-ray simultaneous approach, with both probes exploiting synchrotron radiation sources. In addition, simple experimental layouts that may take advantage of the high brilliance and the wide spectral distribution of the synchrotron radiation emission will be given for specific researches or applications to investigate dynamic processes and non-equilibrium phenomena occurring in many condensed matter and biological systems, of great interest for both fundamental research and technological applications.

Keywords: X-ray; infrared; time-resolved spectroscopy.

1. Introduction

After the early age, when synchrotron radiation (SR) experiments were performed in a few laboratories using light emitted by bending magnets of synchrotrons in the parasitic mode of high-energy experiments, users moved to second-generation dedicated SR facilities where radiation beams at different energy and with different properties were available. Nowadays, neglecting the few operational free-electron lasers, the most advanced accelerators in operation or under construction are the third generation of SR sources. These storage rings have been designed with a large number of straight sections, where special magnetic structures called wigglers and undulators are installed. They are characterized by small and ultra-small electron beams that allow a high-brilliance photon beam to be delivered in a broader spectral range from the far infrared up to the hard X-ray region. The experiments running at SR facilities cover almost all fields of

basic and applied research with a large impact on all sciences and technologies. Because of the enhanced capability of these powerful light sources, applications are continuously expanding, improving the characterization of complex systems and materials and the understanding of the related physico-chemical phenomena. To reconstruct complex phenomena a set of parameters has to be monitored during the process, such as temperature, pH or concentrations. Some parameters are system-specific parameters (*i.e.* of the initial state and of the dynamic evolution) and reaction-specific parameters (such as thermodynamic and kinetic ones). Many of these parameters also depend on the chemical or physical models applied to the system. However, in many processes or reactions and, in particular, when investigating non-equilibrium phenomena, it is difficult to define reliable parameters describing the system. For this reason, in the last years we observed a continuously increasing demand to combine spectroscopic and analytical techniques on the same sample. Although challenging, the combination of vibrational, UV and X-ray methods in a unique experimental set-up with the ultimate spatial and temporal resolutions now available is certainly one of the next frontiers for existing SR sources. It will play an important role in many researches, such as catalytic processes, biological systems and materials science phenomena such as molecular structure dynamics, spin crossover dynamics, *etc.* (Bressler *et al.*, 2009; Radu *et al.*, 2009; Groot *et al.*, 2010; Newton & van Beek, 2010). In the last decade much SR-based research has exploited the advantage of complementary information provided by X-ray techniques and optical methods in the UV/Vis and IR domains mainly using (for the latter methods) conventional sources. In this way we may gain complementary information under identical experimental conditions, minimizing also systematic errors associated with independent experiments performed on the same or different samples. The approach is certainly useful for following fast rate processes, detecting kinetic intermediates *via* complementary but independent observations. New time-resolved and concurrent approaches are required to characterize complex systems, and the combination of a concurrent/simultaneous analysis with a high time-resolution is a key issue to improving our understanding of phenomena evolving under non-equilibrium conditions (Bras *et al.*, 1995; Marcelli *et al.*, 2009*a*). At present, different radiation techniques are rarely carried out simultaneously mainly because of the impossibility of combining instruments and/or sources (Marcelli *et al.*, 2009*a*). Moreover, matching spectra collected with different time-resolved techniques and different instruments is a critical issue. Thanks to the extremely high brilliance of the available SR sources, in particular in the X-ray region, and the availability of fast detectors, the combination of an intense X-ray beam with an IR beam to perform concurrent experiments on the same sample is now possible. The possible combinatorial set-ups, providing access to different but complementary techniques at the same time, will also allow minimizing the time and resources to perform the same experiments in independent runs. Furthermore, they may also guarantee reliable comparisons among experimental data collected on the same sample under the same physical conditions, this being a critical issue for systems under non-equilibrium conditions, for samples changing during an irreversible phase transitions *versus* temperature, pressure or any other physical parameter, or for unique samples available in an extremely limited amount. In addition, in many experiments a heterogeneous distribution occurs in the sample or it is almost impossible to define and reproduce exactly the same initial boundary conditions. Moreover, SR beamline layouts combining an IR and a X-ray beam will make it possible to investigate dynamical processes with a time resolution down to the sub-millisecond regime, resolving plenty of correlated structural, electronic and vibrational phenomena. In this contribution we will present scientific cases from original works and literature reviews to support the proposed IR/X-ray simultaneous approach, with both probes exploiting SR sources and suitable for this new analytical tool, *i.e.* systems where a concurrent/simultaneous characterization may clearly overcome drawbacks and limitations of the existing experimental layouts using conventional sources or designed to run experiments only in a sequential mode. Simple conceptual technical layouts will also be discussed for specific research or applications, such as catalysis.

2. Scientific case of concurrent/simultaneous characterization

2.1. Metal–insulator transitions

A metal–insulator transition (MIT) is a well recognized phenomenon occurring in many condensed-matter systems typically accompanied by large changes in the resistivity. Among the many important MITs are those driven by correlation effects associated with the electron–electron interaction. A Mott insulator is an insulating phase caused by electron correlation (Mott, 1968; Imada *et al.*, 1998). If we now consider a periodic array of atoms, the electronic bandwidth W is the measure of the strength of the interatomic interactions while U is the Coulomb interaction, *i.e.* the measure of the electrostatic energy involved in the creation of polar configurations by transferring an electron from one atom to neighbouring ones. Transport, optical and magnetic properties are frequently quite different from those of ordinary metals and many MITs cannot easily be described within a simple framework.

The interest towards MITs in electronic correlated systems has been mainly triggered by the variety of phenomena observed in transition metal oxides, nickelates, manganites, as well as in cuprate superconductors; among the many, strong spin and orbital fluctuations, mass renormalization effects, incoherence of charge dynamics, and phase transitions tuned by parameters such as band filling, bandwidth and dimensionality. In Fig. 1 we show a schematic phase diagram (adapted by Imada *et al.*, 1998) describing the scenario of a Mott–Hubbard MIT. If we define U as the Coulomb interaction and t the hopping energy, a Mott insulating phase is described by the orange area, at half-filling and when the on-

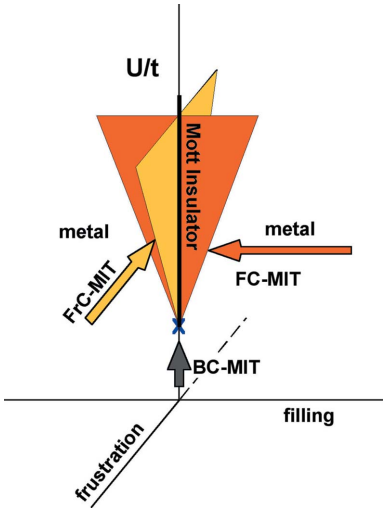

Figure 1
Metal–insulator phase diagram (adapted by Imada *et al.*, 1998) based on the Hubbard model. Because the Mott insulating phase occurs at half-filling and when the on-site Coulomb repulsion U is much larger than the hopping energy t and the associated bandwidth, a transition may occur changing the ratio U/t and/or the filling parameter n. In addition to the filling and bandwidth mechanisms, frustration may also play a role in MITs. With a third coordinate the diagram points out three possible MIT routes: the FC-MIT (filling-control MIT) by doping away from half-filling, the BC-MIT (bandwidth-control MIT) by decreasing the ratio U/t and also a frustration-controlled transition (FrC-MIT).

site Coulomb repulsion U is much larger than the hopping energy t and of the associated bandwidth. Actually, we ideally limit these parameters, a transition to a metallic phase occurs with a mechanism named FC-MIT (filling-controlled MIT), *i.e.* by doping away from half-filling, or with a BC-MIT (bandwidth-controlled MIT), *i.e.* by decreasing the ratio U/t. However, recent research (Powell & McKenzie, 2006) introduced a third MIT mechanism: frustration. As a consequence, in the diagram in Fig. 1 we add a third coordinate: FrC-MIT (*i.e.* frustrated-controlled MIT). Frustration-induced transitions may occur in systems where the presence of competing atomic forces prevents the simultaneous minimization of the interaction energies (Tocchio *et al.*, 2009, and reference therein).

The complexity of the Mott phenomena has been pointed out in great detail by many theoretical studies while from the experimental point of view in the last two decades many *d*-electron compounds have been investigated trying to control the parameters that tune the 'distance' from the MIT. Among the many techniques applied to monitor MITs, high-resolution X-ray diffraction (XRD) experiments should, in principle, determine structural changes at the atomic resolution with a time resolution down to picoseconds (Tanaka *et al.*, 2011). Actually, diffraction does not return information on electronic properties, and using a single probe there is a lack of information about the correlation between atomic and electronic structure changes occurring during a MIT.

From the structural point of view the observed MIT occurring in many transition metal oxides has been associated with a one-dimensional distortion of the periodic lattice, a mechanism knows as Peierls distortion (Peierls, 1955). In other words, MIT occurs as a result of the opening of a band gap at the Fermi energy owing to dimerization processes or small distortions of the regular array that increases the unit-cell length, *i.e.* the atomic positions of the system oscillate so that the perfect order of the one-dimensional crystal is broken. Real systems are very complex often because the presence of inhomogeneities masks the intrinsic properties of the individual phases present in the investigated sample. The interpretation of single sets of experimental data is then *a priori* more challenging.

Looking at experiments available in the literature, vanadium oxide can be considered a prototype system among those where MITs are observed. Many vanadium oxides exhibit temperature-induced MITs, such as the V_2O_3 and the Magneli phases V_nO_{2n-1} ($4 < n < 8$). The VO_2 system shows a MIT at $\sim$340 K, which is characterized by a $3d^1$ configuration and differs from others vanadium oxides because of its non-magnetic ground state and the lack of an antiferromagnetic phase. The MIT is associated with a lattice structural transition from a high-temperature rutile (TiO_2-type) structure (R phase) to a low-temperature monoclinic structure (M_1 phase) (Marezio *et al.*, 1972). V–V pairing occurs in the M_1 phase together with a tilt of the V–V pair. Actually, the origin of the phenomenon can be described as: (i) a Peierls-type transition owing to a structural phase transition from a high-temperature tetragonal metal to a low-temperature monoclinic insulator, in which a bonding–antibonding pair is formed opening the gap, or (ii) a Mott-type transition induced by the strong electron–electron correlation determined by the presence of vanadium atoms. Recent temperature-dependent EXAFS experiments (Yao *et al.*, 2010) before and after the phase transition identified intermediate structural configurations. The data point out the role played by bond angular distortions during the MIT. However, metallic and insulating VO_2 phases were also characterized in the near-IR region ($\sim$5400 cm^{-1} corresponds to an energy gap of $\sim$0.67 eV) because of their different optical responses: fringes in the insulator phase and a broad reflectivity spectrum in the metal phase (Liu *et al.*, 2011), supporting the scenario of a correlated assisted Peierls transition. The emerging scenario points out that subtle structural changes such as the drop of the twisting angle concurrent with a reduction of the resistance by four orders of magnitude trigger the closure of the energy gap (Yao *et al.*, 2010), a mechanism that can be easily monitored by an IR experiment (Liu *et al.*, 2011). However, it has to be clarified whether the two techniques, XAS and IR, probed the same mechanism or just coincidently ran into similar conclusions. A combinatorial X-ray and IR spectroscopic investigation is then mandatory to clarify the MIT issue, although it may work only if experiments will be performed simultaneously on the same sample ruling out the presence of inhomogeneities. It was recently shown in VO_2 using a scattering scanning near-field IR microscope (Qazilbash *et al.*, 2007) that a MIT occurs in a percolation mode. Such inhomogeneous distribution is not restricted to VO_2; other vanadium oxides such as V_2O_3 also exhibit a similar behaviour (Lupi *et al.*, 2010). Data suggest that an inhomogeneous distribution during a phase transition is a

typical condition of many systems where a MIT is observed and the debate on the origin and the occurrence of a MIT is still open in many systems. To improve the understanding of these phenomena, where non-linear responses are clearly associated with dynamic properties of both equilibrium and non-equilibrium states, the only successful approach is a real-time investigation with concurrent structural, electronic and vibrational probes, possibly with a spatial resolution smaller than the size of the characteristic ordered domains inside the sample.

2.2. Characterization of the energy band gap in solid state materials

The energy gap of a solid (Fig. 2, top) is an energy range where no electron states can exist. It generally refers to the energy difference between the top of the valence band and the bottom of the conduction band in insulators and semiconductors. Many functional applications are based on the energy gap of a material, *e.g.* opening the window for solar-energy absorption in a solar-cell battery (Cook *et al.*, 2010), determining the charge conductivity of semiconductors, governing the transport thermopower in thermoelectrics, possessing intrinsic correlations with the superconductivity at low temperature, *etc.* Investigating the energy gap of functional materials is then fundamental not only to understand the variation of the energy gap under different conditions, such as pressure, temperature, magnetic field (Sheregii *et al.*, 2009), but also to engineer the energy gap to fulfil the specific functional requirements of applications. At present, the state-of-the-art techniques to investigate the band gap are Raman, Fourier-transform IR (FTIR), optical absorption spectroscopy and soft-X-ray techniques (X-ray photoemission spectroscopy, soft-X-ray absorption spectroscopy), but also highly demanding X-ray scattering techniques such as inelastic X-ray scattering (designed for electron dynamics instead of lattice dynamics).

It is well known that the energy gap can be tuned *via* inner or external pressures applied to the investigated system. Moreover, the energy gap of semiconductors is negatively correlated with temperature, as the interatomic spacing increases with the temperature while the interaction among electrons decreases. Therefore, the energy gap parameters change dynamically and in most cases in an irreversible way. To monitor parameters under applied conditions, we really need to develop suitable and versatile probes such as new combinatorial set-ups.

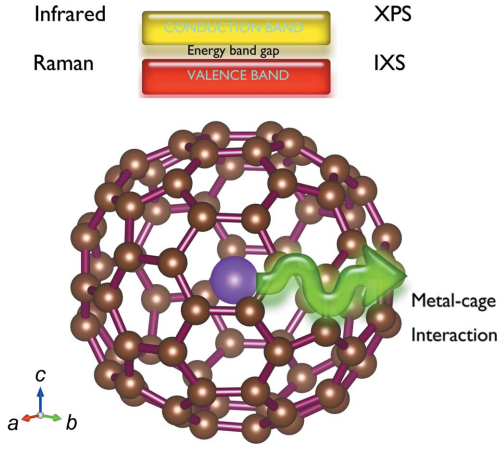

Figure 2
Schematic view of an energy band gap (top) and the metal-cage interaction of an endohedral fullerene (bottom).

2.2.1. IR and X-ray probes of the energy gap. The IR probe is ideal for investigating vibrational states in molecular systems and lattice phonon excitations in solids. Through the interaction between the incident beam and the system, IR-induced excitations can be detected. It is therefore essential to tune the frequency or the energy in the suitable excitation range. IR frequencies go from $\sim$0.3 THz (1.24 meV, $\sim$10 cm^{-1}) to 300 GHz (1.7 eV, $\sim$10000 cm^{-1}), *i.e.* values quite close to the energy gap of both semiconductors and many interesting superconductors.

Although it is absolutely true that X-rays fall in an energy domain greater than any energy gaps, they may easily excite an electron from a bound state to an excited state. X-ray absorption spectroscopy can then indirectly probe the energy band gap owing to the fact that it measures the excitation of electrons from bound states to the continuum. From the energy difference rather than the absolute energy position we may estimate the energy band gap of a system.

The combination of IR and X-ray techniques is not straightforward not only because technical difficulties make simultaneous experiments difficult to implement but also because IR and X-ray photons represent different probes: the IR is sensitive to the molecular composition while X-rays are sensitive to the elements present in the investigated sample. To understand the advantage of the combinatorial set-up, we may consider a real case. Since the conductivity of carbon-based allotropes such as fullerenes, graphene, nanotubes, *etc.* dramatically change with the configuration of carbon atoms, *e.g.* different combinations of graphene layers or zigzag- or arm-chair-type nanotubes with different n, m parameters, it is extremely interesting to determine their electronic band gaps. Most intriguing is the case of the superconductivity observed in the endohedral fullerene (Fig. 2, bottom) with alkaline metals: for instance Cs@C60 that, under high pressure, exhibits superconductivity at 38 K (Ganin *et al.*, 2010). Filling a carbon cage with metal ions is really an ideal case for such a combinatorial set-up. Indeed, because the charge transfer occurring between the interacting components, *i.e.* the metal and the carbon atoms of the cage, can modify both the atomic and the electronic configurations of the system, changes of the energy band gap may occur. At present, no clear understanding of the transport behaviour closely related to the band gap of the system has been achieved; therefore it will be important to reconstruct the dynamics of the anion–cation interaction by means of X-ray absorption and IR spectroscopy. The energy gap is a key issue to determine in order to set up a new Hamiltonian including both the dynamical and the static configurations.

Concurrent experiments have already been performed and two-dimensional correlation plots of X-ray and IR data have

been used to support the identification of fullerene isomers, a challenging and complex problem in metal-doped fullerenes in order to understand the unique properties of these atomic clusters (Marcelli *et al.*, 2009*b*).

2.3. Sol–gel and soft chemistry processes

Sol–gel is a versatile technique that uses liquid phase and mild synthesis conditions to produce monoliths, powders, nanoparticles and films made of pure oxides (*i.e.* silica, titania, zirconia, *etc.*), mixed oxides (silica-titania, silica germania, *etc.*) or hydrid material, that is an organic–inorganic framework (Malfatti & Innocenzi, 2011). Sol–gel can also be combined with colloidal chemistry to induce a controlled structuration on the mesoscale of the final materials. One typical example is the synthesis of self-assembled mesoporous materials by the so-called evaporation-induced self-assembly (EISA) technique (Innocenzi *et al.*, 2009). This technique has been especially applied to the formation of thin films, by spin- or dip-coating. The starting point of the EISA technique is the preparation of a dilute (alcoholic) solution containing the inorganic sol–gel precursors (generally a metal/metalloid alkoxide or salt) and the organic templating agents (surfactant or macromolecular amphiphilic block copolymers). During deposition, because of the solution-substrate wettability, a liquid layer is formed on the substrate, whose thickness depends on the condition of the deposition and the viscosity of the solution. While the solvent evaporates, the amphiphilic molecules reach a critical concentration and form supramolecular structures called micelles. The micelles can have different shapes depending on the surfactant concentration and their interaction with the solvent. At the same time the solvent evaporation triggers the polycondensation of the hydrolyzed sol–gel precursors leading to the formation of an inorganic framework not completely densified. At the end of the evaporation process the film is a nanocomposite formed by the gelation of the starting precursors surrounding an array of micelles. The micelles can be removed from the film afterwards, by thermal annealing or chemical extraction, leaving a porous inorganic or hybrid structure where the pore size and shape have been designed by the micelle dimensions.

Small-angle X-ray scattering (SAXS) has been generally used as the best analytical tool to study the self-assembly of the micelle in film after solvent evaporation, and several studies focused on the *in situ* characterization have been published so far (Falcaro *et al.*, 2005; Malfatti *et al.*, 2006). However, although this technique allows crucial results about the self-organization phenomena occurring in the film during drying to be obtained, it does not provide any information about the chemistry of the process, that is the polycondensation reactions that occur during the transition from sol to gel of the evaporating liquid layer. To overcome this limitation, a combined IR and grazing-incidence SAXS (GISAXS) experiment has been proposed and set to follow *in situ* both the self-assembly of the templating agents in correlation with the kinetics of solvent evaporation and sol–gel precursor polycondensation. The set-up of the experiment is shown in Fig. 3; dip-coater equipment has been installed in the experimental hutch of the Austrian SAXS beamline of the Elettra synchrotron facility. The sol–gel solution used for the experiments was a mixture containing tetraethyl orthosilicate (TEOS) and methyl triethoxysilane (MTES) as a silica source, water and ethanol as the solvents, HCl as the acidic catalyst and the tri-block copolymer Pluronic F127 as the templating agent.

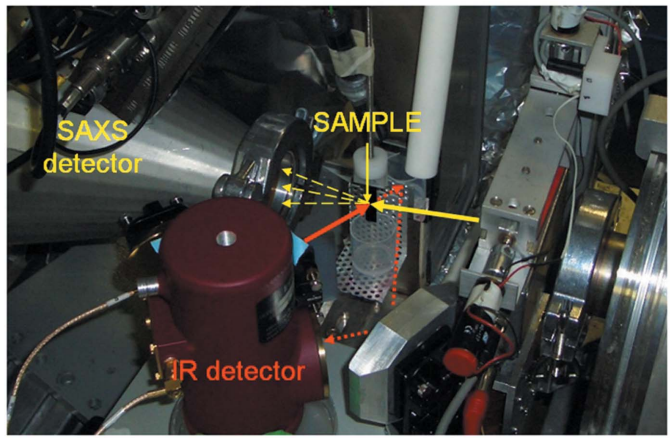

Figure 3
Experimental set-up mounted at the SAXS Austrian beamline at Elettra. [Reproduced with permission from Fig. 1(*b*) of Innocenzi *et al.* (2007).]

GISAXS patterns have been recorded using in-line equipment while FTIR measurements have been performed using the optical system of the IRCube interferometer (Bruker Optics), a compact commercial spectrometer working in the middle-IR with a KBr beamsplitter. The set-up has been designed so that simultaneous IR and GISAXS measurements could be performed on the film, using the conventional globar source and the SR, respectively. The optical components of the FTIR spectrometer have been adjusted so that a parallel IR beam has been focused by an additional external parabolic mirror onto the sample in transmission mode at normal incidence. The transmitted signal has been reflected by a flat mirror towards another elliptical mirror focusing the signal onto the liquid-nitrogen-cooled MCT detector. A GISAXS configuration requires careful setting of the incident angle α_i, because a too small value of α_i could cause total reflection and a too large value could cause insufficient scattering of the sample. Measurements were started immediately after deposition so that all of the evaporation stages of water and ethanol were monitored by IR spectroscopy (Innocenzi *et al.*, 2008).

Fig. 4 shows the GISAXS and IR data sets on the same time scale. Comparison of the results obtained from the two complementary techniques has provided important insight into the structural and chemical aspects of self-assembly. The formation of an ordered mesostructure has been correlated with ethanol and water evaporation from the film; the amount of residual water within the film has been estimated to be 30% in correspondence with the onset of self-assembly, whereas all ethanol has already departed from the film. In addition, a direct correlation between the relative humidity value in the

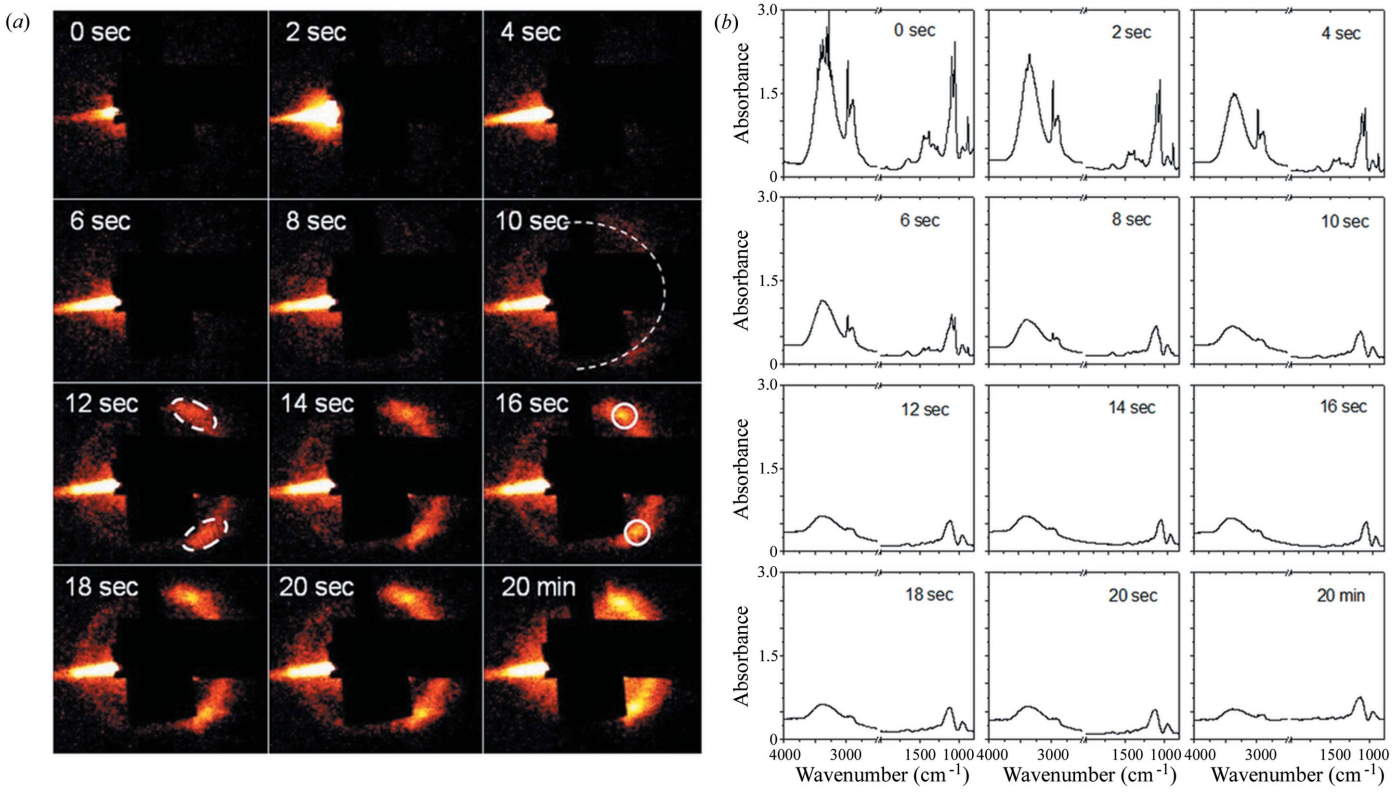

Figure 4
(*a*) SAXS images recorded at different times after the dip-coating. The appearance of a ring after 10 s (beginning of organization) is showed by a dotted line. (*b*) FTIR absorption spectra recorded at different times after the dip-coating. Silicon was used as the substrate. [Reproduced with permission from Figs. 2 and 3 of Innocenzi *et al.* (2007).]

deposition chamber and the quantity of water present in the film has been established for the first time (Innocenzi *et al.*, 2007). The experiment clearly shows the relevance of simultaneous experiments to characterize these processes and the limitation associated with the use of a conventional IR source coupled to a SR source. Indeed, as already pointed out in the early experiments (Bras *et al.*, 1995), to understand the interplay between different mechanisms not only a precise description of the process is required; in addition, to reconstruct the interactions among the components of the system, an accurate correlated control of the time and of the other observables *versus* time is also needed. The huge improvement in the time resolution achieved from the early experiments is remarkable, *i.e.* from hours to seconds. However, in order to resolve many physico-chemical processes further improvements in the order of magnitudes are necessary, and these may only be achievable using SR.

2.4. Real-time monitoring of bone tissue engineering processes

Hydroxyapatite (HA), a calcium phosphate belonging to the group of biocompatible and bioactive ceramics, is the main constituent of the mineral part of bone and teeth tissue. The complex hierarchical structure of bones consists of a supramolecular organic framework (collagen fibrils), playing a role of a pre-organized template, which controls the nucleation of finely divided inorganic clusters, *i.e.* calcium phosphate nanoparticles, from aqueous solution (Mann, 1993). The control of the crystallization process of calcium-phosphate-based particles is really a fundamental issue in materials chemistry applied to biological systems.

The key target of biomaterials research is the preparation of synthetic bone-substitute materials that closely resemble the chemical composition of hard tissues. In recent years, interest in synthetic bone grafts for tissue engineering, such as self-setting calcium phosphate cements, has increased owing to their similarity in composition to bone mineral tissue, biocompatibility, osteoconductive and osteointegration behaviour and the ability to rapidly adapt to the shape of the complex bone defects (Dorozhkin, 2009). That is why calcium phosphate cements, used for non-load-bearing bone fractures and small defects, appear to be very promising materials for bone grafting applications.

Several precursor phases, among them octacalcium phosphate (OCP) and amorphous calcium phosphate (ACP), may participate in biological mineralization to form the final hydroxyapatite phase. The biomineralization mechanism, however, still remains unclear; precursors have to be identified and their functional role has to be clarified (Suzuki *et al.*, 1991). Therefore, an important challenge is *in situ* monitoring of structural transformations occurring to the precursor phases under physiological conditions. For this scope, energy-dispersive X-ray diffraction (EDXRD) and IR techniques

have been applied in separate experiments to follow structural changes taking place in real time. EDXRD may monitor *in situ* the formation of new phases and intermediate products upon the hardening process, allowing to obtain a three-dimensional map of diffraction patterns, collected as a function of the scattering parameter and of time. Together with phase transformations, amorphous *versus* crystalline processes can be followed, and kinetics of crystallization/transformation times can be deduced. Using conventional X-ray sources the typical acquisition time of each pattern is a few minutes, and the overall observation time can be as long as necessary. The energy spectrum of the primary beam produced by a W-anode X-ray tube (operating at 55 keV) of the laboratory experimental technique is modulated by the interaction with the sample. The diffracted radiation is analyzed by an ultra-pure Ge single-crystal solid-state detector, and the reciprocal-space scan, necessary to reconstruct the diffraction pattern, *i.e.* the scan of the scattering parameter $q = aE\sin\theta$ (where q is the normalized momentum transfer magnitude, a is a constant, E is the energy of the incident X-ray beam and 2θ is the scattering angle) is carried out electronically.

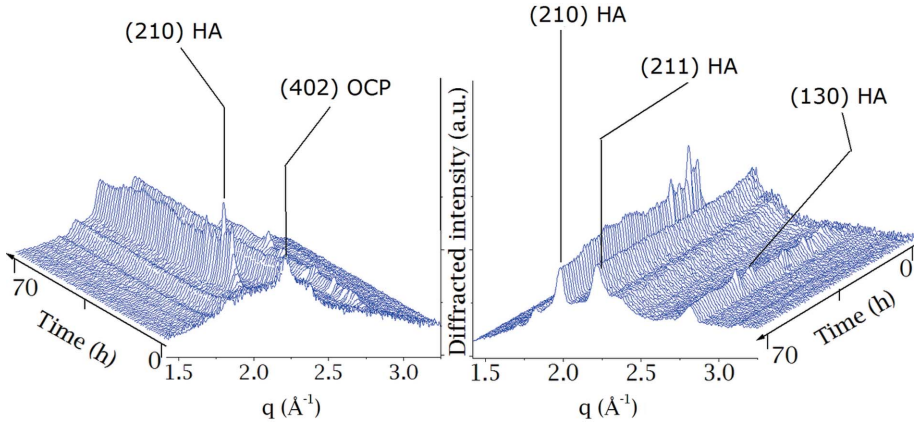

Figure 5
Sequence of EDXRD patterns, collected upon the OCP/hardening-liquid/chitosan (478 kDa) cement. Left: the sequence is shown from the beginning (0 h) to the last (70 h) collected spectrum. Right: the inverse-order sequence.

IR spectroscopy using an IR microscope allows molecular components and structures and their time evolution to be identified. Cement pastes are placed on KBr substrates, and the sequences of spectra can be acquired in the transmittance mode in the mid-IR range at $\sim$8 cm^{-1} resolution. For cement preparation the chitosan biopolymer is usually added to the hardening liquid (Orlov, 2002) (in the proportion of 1:10 by mass) and intensively mixed until a homogeneous mixture is formed. Then, to obtain the cement paste, the cement powder is added to the hardening liquid/chitosan mixture and intimately mixed until a dense homogeneous creamy paste is formed. The liquid-to-powder ratio is $\sim$1:1 by mass. Immediately after preparation, the cement paste is divided into two parts; one of them is investigated by EDXRD, while the other by IR spectroscopy. Drops of simulated body fluid (SBF) are added to the cement paste 15 min after its preparation, reproducing the medical operating room scenario. The chitosan biopolymer characterized by a high molecular weight (478 kDa) is added to the investigated systems, since its presence does not alter the final product (HA), the only effect being a lengthening of the crystallization times. Using conventional sources, this is often necessary in order to better follow the evolution from the starting reagents to the products (Smirnov *et al.*, 2010). Furthermore, large polymer molecules of biocompatible and biodegradable chitosan may induce the orientation of calcium phosphate precipitates in a specific direction. As already pointed out, clarifying how biopolymer macromolecules act upon the precipitation of calcium phosphate phases is a key issue for designing biomimetic routes for producing self-organized materials.

2.4.1. OCP/hardening-liquid/chitosan and OCP/hardening-liquid/chitosan/SBF systems. In Fig. 5 we show two three-dimensional maps of EDXRD patterns of the OCP/hardening-liquid/chitosan (478 kDa) collected as a function of both scattering parameter (q) and time (t). The overall observation time was 70 h and the patterns were collected every 15 min. Remarkable changes take places during the hardening process and new peaks, such as (210) at q = 1.99 Å^{-1}, (211) at q = 2.25 Å^{-1} and (130) at q = 2.76 Å^{-1}, attributable to the HA phase, appear after approximately 3 h from the beginning of the experiment. Moreover, other important changes occur during the entire hardening process, such as the intensity modulation of the two Bragg reflections [(210) and (130)], undergoing a fast increase and decrease of the diffracted intensity. This modulation could be associated with structural changes occurring in the system that have to be better investigated and understood.

Available literature data (Aimoli *et al.*, 2008) point out that the cooperative action of chitosan and SBF induces the formation of a preferentially oriented HA phase, this process being similar to the oriented self-assembling process in collagen–apatite matrix in human plasma, occurring upon *in vivo* biomineralization. Biopolymers may possibly interact in order to conduct ions to molecular recognition, leading epitaxy to orient crystals. For this reason a few drops of SBF can be added to the cement paste. In Fig. 6, two three-dimensional maps of EDXRD patterns, collected upon the OCP/hardening-liquid/chitosan/SBF cement paste, are presented. New reflections, appearing after approximately 90 h, can be well distinguished in the final patterns of the process and assigned to a crystalline HA phase. Accordingly, all the detected reflections are attributed and labelled with proper HA Miller indices.

2.4.2. ACP/hardening-liquid/chitosan system. It is also useful to present the results of the investigation of the amorphous calcium phosphate bone cement hardening process. In

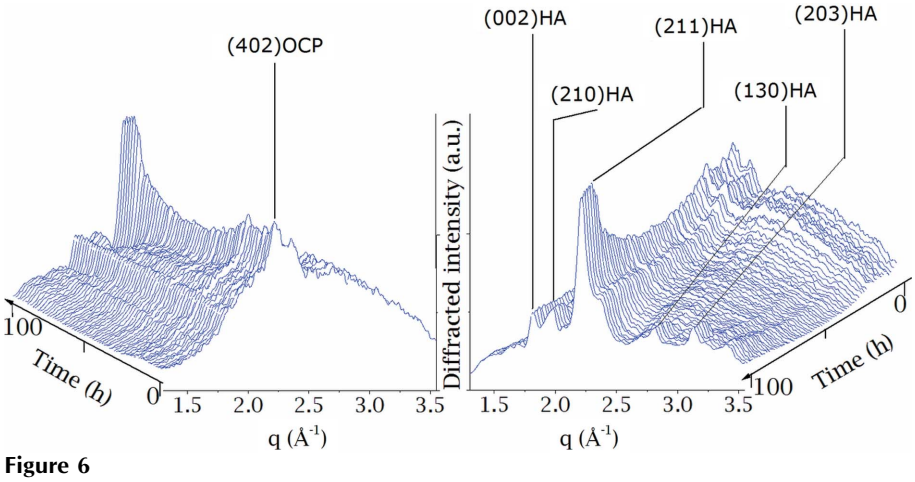

Figure 6
Sequence of EDXRD patterns, collected upon the OCP/hardening-liquid/chitosan (478 kDa)/SBF cement. Left: the sequence is shown from the beginning (0 h) to the last (100 h) collected pattern. Right: the inverse-order sequence.

this case we have obtained experimental evidence of the octacalcium phosphate intermediate phase during the sequential conversion from amorphous calcium phosphate into hydroxyapatite. As can be seen from Fig. 7 (top), the OCP phase (the most intense peak at q = 1.95 Å^{-1}) appears approximately 7 h after the cement paste preparation and disappears after ∼17 h. The final HA phase (peaks at q = 1.99 Å^{-1} and 2.81 Å^{-1}) is detected approximately 12 h after the paste preparation and coexists with the initial ACP phase until the end of the experiment. The co-presence of the initial phase indicates that under these experimental conditions the transition process is not complete. In Fig. 7 (bottom) we show the IR spectrum and the appearance of the OH^- band at 3220 cm^{-1} accounting for the HA formation after −28 h from the cement hardening. It is clearly correlated with EDXRD data (top panel of Fig. 7) being the maximum of HA diffracted intensity detected approximately at the same time. A similar result was also observed for poorly crystalline apatite cement and chitosan (38 kDa) (Rau *et al.*, 2010).

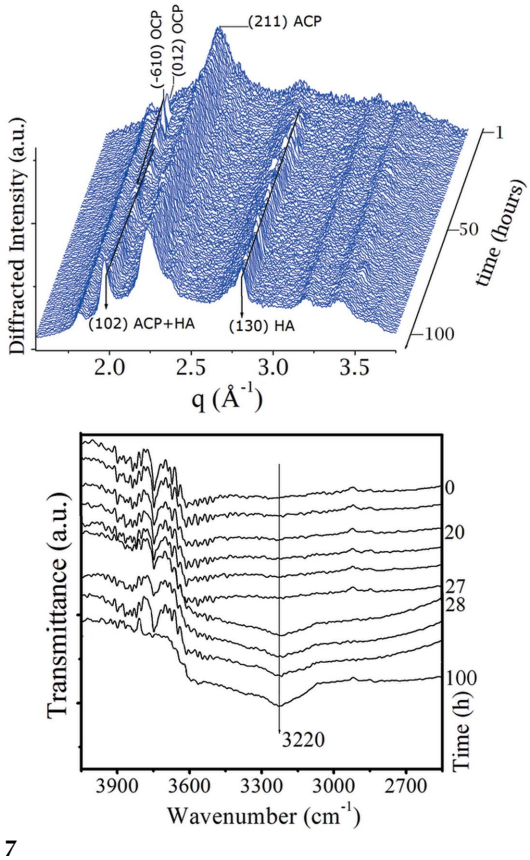

Figure 7
Top: sequence of EDXRD patterns, collected upon the ACP/hardening-liquid/chitosan (478 kDa) cement. The formation of the new OCP phase is shown. Bottom: sequence of FTIR spectra of the same cement composition.

To summarize, a concurrent/simultaneous approach can be applied to the investigation of structural transformations and hardening processes in various cement systems. X-ray diffraction demonstrates the sequential conversion of the ACP into the HA structure, while IR provides additional chemical information supporting the structural analysis. Although consistent, the main drawbacks of these studies are the limited spatial and time resolution and a non-negligible background owing to the use of laboratory radiation sources. As a consequence, only the most intense peaks can be resolved and monitored. Performing the same experiments with SR could be more effective not only due to the enhanced time and spatial resolution. Indeed, with time-resolved X-ray and IR concurrent analysis, it will be possible to investigate dynamical processes related to the chemical transformations with a time resolution down to the sub-millisecond regime allowing a deeper understanding of biomineralization mechanisms occurring during the hard tissue formation.

2.5. The photo-activation process of rhodopsin

Rhodopsin is the photoreceptor of retinal rod cells that initiates the visual cascade. It is the prototype of class A G-protein coupled receptors, a class that comprises hundreds of proteins, like the β-adrenergic receptor, odor or hormone receptors. Like rhodopsin, all these proteins consist of seven-transmembrane helices. Their common function is to transmit a signal to a G-protein. Whereas most of these receptors are activated by ligand binding, light absorption in rhodopsins dark state (Rho) causes isomerization of the prostetic group 11-*cis* retinal, bound to the apoprotein *via* a protonated Schiff base, to straightened all-*trans* retinal (Hubbard & Wald, 1952). This in turn triggers conformational changes of the protein, such as backbone alterations or protonations/deprotonations of carbonyl groups and secondary structure alterations, which finally lead *via* intermediates to the active G-protein inter-

acting species Metarhodopsin II (Meta II) within milliseconds. Upon its formation, deprotonation of the retinal Schiff base causes a strong blue shift of the visible absorption maximum. Subsequently, large conformational alterations including an outward tilt of helix VI occur to open a cleft that enables G-protein binding (Farrens *et al.*, 1996). Fig. 8 (left) compares the dark state structure as solved by X-ray crystallography (Palczewski *et al.*, 2000) (blue) with the crystallized active form Meta II (Choe *et al.*, 2011) (red). The crystal structures of both the ligand-free opsin apoprotein (Park *et al.*, 2008) and the active Meta II state (Choe *et al.*, 2011) provide information about the intramolecular couplings that stabilize this intermediate. Information about the dynamics of its formation and thus the proper interaction of several functional groups within the protein can be derived by simultaneous time-resolved UV/Vis and FTIR difference spectroscopy which allows the Schiff base protonation state and structural alterations of the protein, respectively, to be monitored. Recently, the structural impact of single amino acids, *i.e.* the function of highly conserved Tyr-223, which only after protonation of Glu-134 can interact with Arg-135, was investigated using this spectroscopic technique (Elgeti *et al.*, 2011).

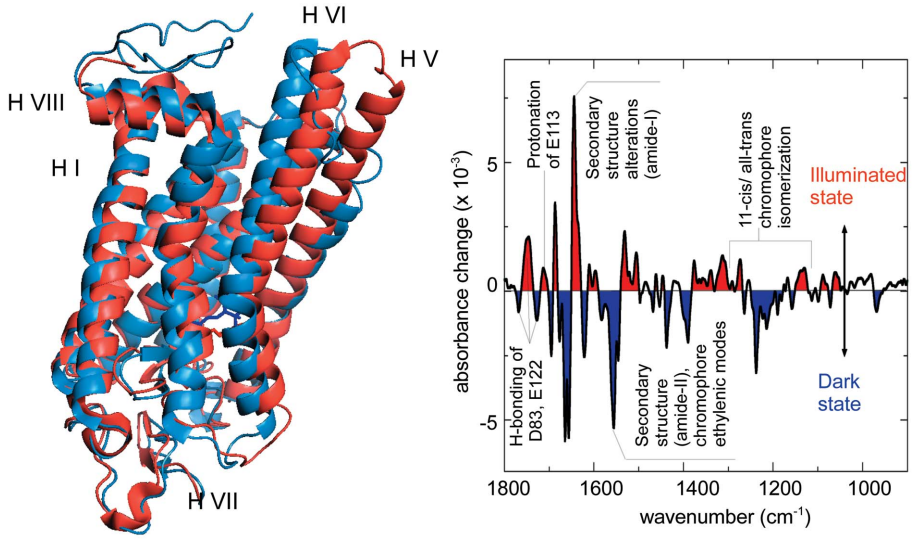

Figure 8
Left: structure of the rhodopsin dark state (blue) and the G-protein interacting Meta II state (red). The outward tilt of helix VI (H VI) opens a cleft on the cytosolic side that is a prerequisite for interaction with the G-protein. Right: FTIR difference spectrum of Meta II formation, calculated as Meta II minus rhodopsin absorbance spectrum. Negative bands (blue) occur owing to vibrational modes of the dark state while positive bands are caused by the illuminated state. Important spectral regions, indicative of protonated carbonyl, protein secondary structure alterations and chromophore isomerization are described.

In the dark, Meta II decays irreversibly *via* the species Meta III by hydrolysis of the retinal Schiff base (Matthew *et al.*, 1963). Even illumination with UV light does not restore the dark state but also leads to the formation of Meta III (Bartl *et al.*, 2001). Hence, fresh receptor must be regenerated by metabolically supplied 11-*cis* retinal provided by an energy- and resource-consuming metabolism, the retinoid cycle (Lamb & Pugh, 2004).

A major scientific aim is to gain further insight into the intramolecular interactions that contribute to and control Meta II formation. This can be done by vibrational spectroscopy, which is an important tool for obtaining structural information about such conversions (Siebert, 1995) (Fig. 8, right). However, on the one hand, conventional FTIR spectroscopy is limited to a time resolution of a few milliseconds and it is therefore not sufficient to fully resolve the activation process. On the other hand, the advanced step-scan technique which is normally used to obtain spectra in the fast time range (microseconds to nanoseconds) cannot be applied since it requires cyclic systems, such as bacteriorhodopsin, which after light excitation returns to the initial dark state within milliseconds (Rödig *et al.*, 1999). Therefore, to investigate these processes in non-cyclic vertebrate rhodopsin a dispersive microsecond single-shot IR spectrometer is under development. However, spectral acquisition requires a signal-to-noise ratio of 1000 or better even in a single-shot mode. This is only possible using available mercury cadmium telluride line array detectors by taking advantage of high-brilliance IR SR sources. Moreover, SR allows diffraction-limited optics to be used, thereby optimally filling the spectrometer entrance aperture. Additionally, it provides the possibility to use narrow-band UV/Vis pulses from the storage ring to trigger the photo-process of the protein. A simultaneous recording of all IR detector pixels in snap-shot mode cancels out excess signal noise introduced from the storage ring environment and allows the whole spectrum to be recorded within a microsecond time-scale. Within this framework it will be possible to fully resolve the late Meta transitions of rhodopsin. Concurrent time-resolved experiments will be fundamental to monitor such processes thereby improving the understanding of rhodopsins late activation steps and complementing the knowledge available from X-ray crystallography, structural information and details of electronic structure, obtainable with elemental specificity using XAS and XES spectroscopy.

2.6. DRIFTS/transmission X-ray experiments for catalysis

IR spectroscopy offers three possibilities for studying materials such as high area heterogeneous catalysts: transmission attenuated total reflection (ATR) and diffuse reflectance infrared Fourier transform spectroscopy (DRIFTS). In terms of the synchronous combination of IR spectroscopy with X-ray probes for the study of the structure and reactivity of catalysts, to date, it is the latter (Newton, 2009; Kubacka *et al.*, 2009; Ferri *et al.*, 2010; Korhonen *et al.*, 2011; Marinkovic *et al.*, 2011*a*,*b*; Becker *et al.*, 2011; Lee *et al.*, 2011) that has been the most exploited when this couple was first demonstrated

(Newton *et al.*, 2004). Transmission EXAFS coupled to transmission IR has recently been demonstrated (Bando *et al.*, 2009, 2012), and indeed may be better adapted than DRIFTS to certain situations: DRIFTS readily permits coupling to X-ray measurements made in transmission and/or back-scattering geometries but is much less obviously suited to situations that require the detection of X-rays in directions orthogonal to the X-ray path (such as fluorescent-yield XAFS and emission spectroscopy). For more details combining DRIFTS/X-ray, as well as other X-ray/IR couples, see Newton *et al.* (2010, 2012*a*). Nonetheless, thus far DRIFTS has been the IR variant of choice for combined X-ray/IR studies of heterogeneous catalysts and has been shown to be compatible with synchronous coupling to transmission scanning (Newton, 2009; Korhonen *et al.*, 2011; Marinkovic *et al.*, 2011*a*,*b*) or dispersive (Ferri *et al.*, 2010; Becker *et al.*, 2011; Lee *et al.*, 2011) EXAFS and latterly hard X-ray diffraction (Newton *et al.*, 2010, 2012*b*).

2.6.1. Sample environment for kinetic studies of catalysing using DRIFTS and transmission X-ray methods. Taking the former, first we might make certain observations within the overall remit of this paper. The first is that even with current commercial spectrometers making it possible to collect IR spectra in a single shot, on time scales of tens of milliseconds at resolutions (2 to 4 cm^{-1}) to a first approximation, this is more than acceptable for the majority of heterogeneous catalysis research. This level of performance is not, in the first instance, the limiting factor in most *in situ* applications though, as will be discussed below, as what one can obtain in a single shot with such acquisition times using currently available spectrometers and sources does need to be eventually considered.[1]

We might note that for more static steady-state measurement, many systems [with the possible exception of the Spectratech high-temperature high-pressure (HT–HP) dome] may be relatively easily modified for transmission X-ray work (Newton, 2009; Marinkovic *et al.*, 2011*a*,*b*). Some very commonly used commercial systems, such as the Harrick Praying Mantis, carry with them relatively large internal dead volumes ($\sim$14 cm^3) and therefore are of limited utility in transient studies. Others (for instance Spectratech) are better in this respect. For instance, Meunier and co-workers (Meunier *et al.*, 2008) have shown that the design of the Spectratech HT–HP accessory, whilst permitting high-pressure (to 100 bar) experimentation, inadvertently restricts gas flow and mixing above the sample such that it is of limited utility for transient work in the as-purchased set-up.

From a purely IR and process perspective, there have been attempts to ameliorate such weaknesses using a variety of bespoke modifications (Newton, 2009; Meunier *et al.*, 2008; Santo *et al.*, 2005; Schubert *et al.*, 2001) designed to reduce dead volumes and improve the time constants and gas flow characteristics intrinsic to the cells. In terms of intrinsic time constant, however, the best solution that has been demonstrated for DRIFTS is that owing to McDougall *et al.* (Cavers *et al.*, 1999). This design is predicated on a maximal elimination of extraneous volume to the point where it is difficult to see how one might advance further in this direction. Indeed, it was a copy of this cell configuration that was initially employed to fuse DRIFTS with the time-resolving X-ray probe of dispersive EXAFS (Newton *et al.*, 2004); as transmission EXAFS brings with it no significant solid angle requirements for detection of the X-rays, this sort of 'flat top' cell is perfectly amenable to such a combined experiment.

Equally though within this configuration some price is paid in the achievable terms of upper operating temperature and a non-plug-flow flow configuration; it is also not easily compatible with X-ray techniques where obtaining a minimal solid angle of X-ray detection is an issue. This is why the recent combinations of DRIFTS with X-ray diffraction (Newton *et al.*, 2010, 2012*b*) have used a modified version of the Spectratech HT–HV (high vacuum) DRIFTS cell (Newton, 2009; Newton *et al.*, 2010, 2012*a*): this design does bring with it an increased dead volume (to $\sim$2.5–3 cm^{-3} after modification) but does permit diffraction data to be obtained when using X-rays of a sufficiently high energy [$\sim$90 keV in the examples demonstrated to date (Newton *et al.*, 2010, 2012*b*)].

One area where further advances could therefore be made is in designing a low-volume DRIFTS cell that permits a much larger solid angle for X-ray detection to be attained. This would allow a wider range (to lower energies) of X-ray energies to be used for the diffraction component of the combined experiment but also bring with it the possibility of combining total X-ray scattering methods [with the associated pair-distribution-function (PDF) measurements of analysis (Gallezot *et al.*, 1984; Ferri *et al.*, 2010; Egami & Billinge, 2003; Petkov, 2008)] with DRIFTS.

The maturation of third-generation X-ray sources, associated insertion devices and detector technology has recently also made total X-ray scattering become tractable as a time-resolving structural-kinetic technique for *in situ* research into catalyst behaviour (Chupas *et al.*, 2007; Zhao *et al.*, 2011; Newton *et al.*, 2012*a*). To achieve this, however, a large amount [as a rule of thumb to $\sim$25–30 Q ($Å^{-1}$), corresponding to $\sim$45° angle to be collected at 60 keV] of high-quality scattering data is required to be obtained. As such, to realise this seductive X-ray/DRIFTS couple, a dedicated set-up is required. A modified version of the Harrick Praying mantis has been tested [at sector 11-IDB, Advanced Photon Source (APS)] for a combined PDF/DRIFTS capacity. However, and as stated above, this DRIFTS accessory is poorly adapted for very fast transient experimentation. As such, an entirely new design is currently being developed (collaboration between ESRF and the APS) and will be tested/demonstrated in the very near future. The completion of this latest design project should result in an apparatus that may be used with equani-

[1] We note that the same is true in X-ray experiments. For instance, both dispersive and quick-scanning methods have been developed and demonstrated to be capable of acquiring data with similar spectral repetition rates. However, the available flux is only one of the many parameters including the nature of the sample that contribute to determine a suitable data acquisition. Despite headline time resolutions on the millisecond level often being found in the literature, inspection often shows that the actual acquisition times required for useful/justifiable deductions to be made are in reality significantly longer.

mity for combining DRIFTS with a range of transmission hard X-ray techniques.

2.6.2. Limiting factors relating to IR and DRIFTS instrumentation. The use of conventional IR sources and commercially available DRIFTS optics, however, leads to some further limiting factors to the application of such methods to the widest range of problems where they might find utility. When considering combined and dynamic DRIFTS/X-ray measurements in catalysis this is an important issue for the following reason: for any transmission X-ray experiment there is an optimal X-ray path length through which the X-rays need to traverse, and within the target area presented by such samples to the IR there needs to be sufficient IR flux to yield usable data on the time scale required.

X-ray scattering techniques favour short path lengths (at most 2–3 mm) to avoid multiple-scattering effects and the physical projection of the depth of the sample onto the obtained scattering data at high scattering angles. In XAFS, the optimal path length required to make a measurements is a convolution of the energy of the elemental edge to be probed and the overall composition and density of the sample. Many catalysts are founded upon elements that have absorption edges in the sub-10 keV region, *e.g.* the entire first-row transition metal elements. Moreover, support or promoter materials, which absorb and scatter X-rays very well, may be extremely prevalent in catalyst formulation. Both of these effects cause the usable transmission path length to dwindle to dimensions of 2 mm or much less. As such, for the study of the majority of possible catalyst formulations, the DRIFTS component needs to be constrained and targeted into a dimension at the sample of $\sim$<2 mm in diameter. Further, if one wishes to consider the possibility of making combined IR/X-ray scattering measurements on working single-crystal catalyst bodies (for instance zeolites), and without going to a IR microscope configuration, then dimensions much smaller than this need to be envisaged.

Two obvious strategies present themselves: (i) the implementation of more brilliant (smaller, brighter) sources; or (ii) a novel rearrangement of the DRIFTS experiment itself. In terms of the former option, as with sample environment, widespread commercialization tends to lead to a standardization along the ends of long-term reliability than extreme performances: bench-top spectrometers are uniformly supplied with standard sources. However, extremely stable and much more brilliant (by factors of $>10^4$ in the mid-and far-IR) IR sources are available in the same places (synchrotrons) that produce extremely brilliant X-rays. Indeed, the use of SR IR light has been, and continues to be, widespread in the far-IR and for mid-range IR microscopy.

To this day, however, whilst there are dedicated IR lines and side stations at just about every SR facility currently in operation, there is not a single example of a beamline configuration wherein the IR part of the electromagnetic spectrum is extracted and then combined in the same place as its shorter-wavelength cousin.

This situation seems not to be a question of feasibility: at ID21 at the ESRF, for example, everything save for the last recombinative step was achieved by 2005 (http://www.esrf.fr/UsersAndScience/Experiments/Imaging/ID21/). Here though, the IR light taken from the fan of an adjacent bending magnet is only used to create a side station for conventional IR microscopy rather than being used to create a new type of dichroic experiment. Alternatively, one could envisage taking both the X-rays and the IR fan from the same front-end within a single beamline. Though technically much more demanding than utilizing an adjacent bending magnet, this is still a plausible option, to the extent that at least one design that does exactly this has been considered and discussed in some detail (Marcelli *et al.*, 2010).

The current upgrade of ID24 at the ESRF (dispersive EXAFS) has yielded the opportunity to investigate a new development, made in collaboration with Varian (now Agilent) and OMT Solutions (Eindhoven). A schematic of this new optical layout is given in Fig. 9. The principal design objective of this new arrangement is to realise a sub-1 mm focal spot whilst retaining maximum IR throughput, *i.e.* no use of internal attenuators, at suitable resolution (2–4 cm^{-1}). The specific details of how this is realised, along with an assessment of the performance of this new optical layout, will be published elsewhere (Newton *et al.*, 2012*c*). However, here we simply note that in order to achieve the desired ends a new optical configuration for the DRIFTS experiment has to be adopted.

In this new configuration illumination of the sample and detection of the IR light scattered from it are now made along the same path. This is made possible through the use of a novel and proprietary beamsplitter arrangement. By coupling this with a sample environment similar to that used in the original DRIFTS/EXAFS experiment, and founded upon the design ideas of McDougall *et al.* (Cavers *et al.*, 1999), a position

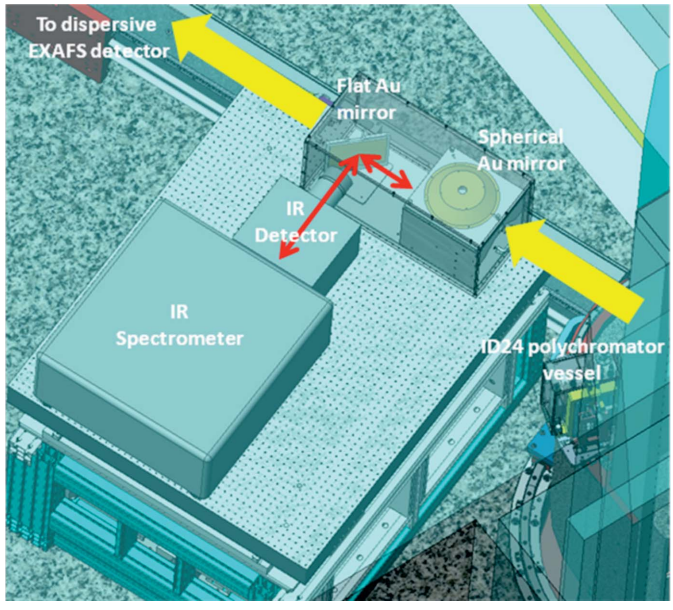

Figure 9
Schematic layout of a new type of DRIFTS/EXAFS experiment to be permanently installed/available on the 'large (X-ray) spot' branch of the upgraded ID24 at the ESRF.

should be reached wherein currently intractable samples that require <2 mm transmission X-ray path lengths should become amenable to this type of methodology. Moreover, this may be done with minimal compromises made in respect of either (X-ray or IR) components of the experiment (Newton *et al.*, 2010, 2012*a*). Of secondary note is that this configuration hypothetically leads to some further experimental possibilities beyond the specification originally outlined. The hole placed in the centre of the spherical top mirror sits within a small solid angle delineated by the sample environment itself. This solid angle can therefore be used without compromising the rest of the experiment. As such the hole has been placed here to provide a port where further experiments can be added and give yet more experimental capacity or ability to observe other aspects of the materials behaviour whilst training the simultaneous IR/XAS viewpoint. One might think of using this port, together with a suitably windowed DRIFTS cell, for UV excitation.

3. Conclusion

We presented here a series of experiments and phenomena that can be usefully investigated and characterized exploiting novel conceptual layouts where IR and X-ray SR beams can be delivered simultaneously to the same sample. Time-resolved and simultaneous measurements on non-equilibrium systems or complex physico-chemical phenomena may indeed allow a reconstruction not possible using a single technique and that remains challenging also combining different data collected by independent sequential experiments. In the last decade the demand of a combinatorial approach has continuously increased and the potential applications are certainly larger than the limited number of examples given in this contribution. Here, we briefly presented and discussed a few representative applications from biology to materials science that may certainly take benefit from the future availability of dedicated instruments with concurrent time-resolved analytical capabilities. An accurate discussion has been given in particular for catalytic applications.

One of us (WX) acknowledges the financial support of the National Natural Science Foundation of China (grant No. 11105172). MAN would like to acknowledge the continued support of the ESRF that has permitted the development and implementation, for the benefit of the wider user community, of novel experiments based upon the synchronous application of X-rays and IR spectroscopy. The Royal Society of Chemistry is thanked for the journals grant (09 01 639) that initiated collaboration with Peter Chupas at the APS, and the APS is thanked for a subsequent visiting scientist position (2010/2011). Professor John Evans and Andrew Dentare are sincerely thanked for their contribution to the [EPSRC (UK) funded] design and construction of the original DRIFTS/EXAFS experiment constructed at the University of Southampton (UK).

References

Aimoli, C. G., De Lima, D. O. & Beppu, M. M. (2008). *Mater. Sci. Eng. C*, **28**, 1565–1571.
Bando, K. K., Wada, T., Miymoto, T., Miyazaki, K., Takakusgi, S., Gott, T., Yamaguchi, A., Nomura, M., Oyama, S. T. & Asakura, K. (2009). *J. Phys. Conf. Ser.* **190**, 012158.
Bando, K. K., Wada, T., Miymoto, T., Miyazaki, K., Takakusgi, S., Gott, T., Yamaguchi, A., Nomura, M., Oyama, S. T. & Asakura, K. (2012). *J. Catal.* In the press.
Bartl, F. J., Ritter, E. & Hofmann, K. P. (2001). *J. Biol. Chem.* **276**, 30161–30166.
Becker, E., Carlsson, P. A., Kylhammara, L., Newton, M. A. & Skoglundh, M. (2011). *J. Phys. Chem. C*, **115**, 944–951.
Bras, W., Derbyshire, G. E., Bogg, D., Cooke, J., Elwell, M. J., Komanschek, B. U., Naylor, S. & Ryan, A. J. (1995). *Science*, **267**, 996–999.
Bressler, Ch., Milne, C., Pham, V. T., Elnahhas, A., van der Veen, R. M., Gawelda, W., Johnson, S., Beaud, P., Grolimund, D., Kaiser, M., Borca, C. N., Ingold, G., Abela, R. & Chergui, M. (2009). *Science*, **323**, 489–492.
Cavers, M., Davidson, J. M., Harkness, I. R., Rees, L. V. C. & McDougall, G. S. (1999). *J. Catal.* **188**, 426–430.
Choe, H. W., Kim, Y. J., Park, J. H., Morizumi, T., Pai, E. F., Krauss, N., Hofmann, K. P., Scheerer, P. & Ernst, O. P. (2011). *Nature (London)*, **471**, 651–655.
Chupas, P. J., Chapman, K. W., Jennings, G., Lee, P. L. & Grey, C. P. (2007). *J. Am. Chem. Soc.* **129**, 13822–13824.
Cook, T. R., Dogutan, D. K., Reece, S. Y., Surendranath, Y., Teets, T. S. & Nocera, D. G. (2010). *Chem. Rev.* **110**, 6474–6502.
Dal Santo, V., Dossi, C., Fusi, A., Psaro, R., Mondelli, C. & Recchia, S. (2005). *Talanta*, **66**, 674–682.
Dorozhkin, S. V. (2009). *Materials*, **2**, 221–291.
Egami, T. & Billinge, S. J. L. (2003). *Underneath the Bragg Peaks: Structural Analysis of Complex Materials.* New York: Pergamon Press.
Elgeti, M., Kazmin, R., Heck, M., Morizumi, T., Ritter, E., Scheerer, P., Ernst, O. P., Siebert, F., Hofmann, K. P. & Bartl, F. J. (2011). *J. Am. Chem. Soc.* **133**, 7159–7165.
Falcaro, P., Costacurta, S., Mattei, G., Amenitsch, H., Marcelli, A., Guidi, M. C., Piccinini, M., Nucara, A., Malfatti, L., Kidchob, T. & Innocenzi, P. (2005). *J. Am. Chem. Soc.* **127**, 3838-3846.
Farrens, D. L., Altenbach, C., Yang, K., Hubbell, W. L. & Khorana, H. G. (1996). *Science*, **274**, 768–770.
Ferri, D., Kumar, M. S., Wirz, R., Eyssler, A., Korsak, O., Hug, P., Weidenkaff, A. & Newton, M. A. (2010). *Phys. Chem. Chem. Phys.* **12**, 5634–5646.
Gallezot, P. (1984). *X-ray Techniques in Catalysis* in *Catalysis, Science and Technology*, edited by J. R. Anderson and M. Boudart, Vol. 5, ch. 4. Berlin: Springer.
Ganin, A. Y., Takabayashi, Y., Jeglic, P., Arcon, D., Potocnik, A., Baker, P. J., Ohishi, Y., McDonald, M. T., Tzirakis, M. D., McLennan, A., Darling, G. R., Takata, M., Rosseinsky, M. J. & Prassides, K. (2010). *Nature (London)*, **466**, 221–225.
Groot, F. M. de, de Smit, E., van Schooneveld, M. M., Aramburo, L. R. & Weckhuysen, B. M. (2010). *Chem. Phys. Chem.* **11**, 951–962.
Hubbard, R. & Wald, G. (1952). *J. Gen. Physiol.* **36**, 269–315.
Imada, M., Fujimori, A. & Tokura, Y. (1998). *Rev. Mod. Phys.* **70**, 1039–1263.
Innocenzi, P., Malfatti, L., Costacurta, S., Kidchob, T., Piccinini, M. & Marcelli, A. (2008). *J. Phys. Chem. A*, **112**, 6512–6516.
Innocenzi, P., Malfatti, L., Kidchob, T., Costacurta, S., Falcaro, P., Piccinini, M., Marcelli, A., Morini, P., Sali, D. & Amenitsch, H. (2007). *J. Phys. Chem. C*, **111**, 5345.
Innocenzi, P., Malfatti, L., Kidchob, T. & Falcaro, P. (2009). *Chem. Mater.* **21**, 2555–2564.
Korhonen, S. T., Beale, A. M., Newton, M. A. & Weckhuysen, B. M. (2011). *J. Phys. Chem. C*, **115**, 885–896.

Kubacka, A., García, M. F., Arias, A. M. & Newton, M. A. (2009). *Catal. Today*, **145**, 288–293.
Lamb, T. D. & Pugh, E. N. (2004). *Prog. Retin. Eye Res.* **23**, 307–380.
Lee, A. F., Ellis, C. V., Naughton, J. N., Newton, M. A., Parlett, C. M. & Wilson, K. (2011). *J. Am. Chem. Soc.* **133**, 5724–5727.
Liu, W. T., Cao, J., Fan, W., Hao, Z., Martin, M. C., Shen, Y. R., Wu, J. & Wang, F. (2011). *Nano Lett.* **11**, 466–470.
Lupi, S., Baldassarre, L., Mansart, B., Perucchi, A., Barinov, A., Dudin, P., Papalazarou, E., Rodolakis, F., Rueff, J. P., Itié, J. P., Ravy, S., Nicoletti, D., Postorino, P., Hansmann, P., Parragh, N., Toschi, A., Saha-Dasgupta, T., Andersen, O. K., Sangiovanni, G., Held, K. & Marsi, M. (2010). *Nat. Commun.* **1**, 105.
Malfatti, L. & Innocenzi, P. (2011). *J. Sol-Gel Sci. Technol.* **60**, 226–235.
Malfatti, L., Kidchob, T., Costacurta, S., Falcaro, P., Schiavuta, P., Amenitsch, H. & Innocenzi, P. (2006). *Chem. Mater.* **18**, 4553–4560.
Mann, S. (1993). *Nature (London)*, **365**, 499–505.
Marcelli, A., Hampai, D., Wei, X., Malfatti, L. & Innocenzi, P. (2009*a*). *Acta Phys. Pol. A*, **115**, 489–500.
Marcelli, A., Wei, X., Lei, L., Chunru, W., Chu, W. & Wu, Z. Y. (2009*b*). *J. Nanophoton.* **3**, 031975.
Marcelli, A., Xu, W., Hampai, D., Malfatti, L., Innocenzi, P., Schade, U. & Wu, Z. (2010). *Anal. Bioanal. Chem.* **397**, 2095–2108.
Marezio, M., McWhan, D. B., Remeika, J. P. & Dernier, P. D. (1972). *Phys. Rev. B*, **5**, 2541–2551.
Marinkovic, N. S., Wang, Q., Barrio, L., Ehrlich, S. N., Khalid, S., Cooper, C. & Frenkel, A. I. (2011*a*). *Nucl. Instrum. Methods Phys. Res. A*, **649**, 204–206.
Marinkovic, N. S., Wang, Q. & Frenkel, A. I. (2011*b*). *J. Synchrotron Rad.* **18**, 447–455.
Matthew, R. G., Hubbard, R., Brown, P. K. & Wald, G. (1963). *J. Gen. Physiol.* **47**, 215–240.
Meunier, F. C., Goguet, A., Shekhtman, S., Rooney, D. & Daly, H. (2008). *Appl. Catal. A*, **340**, 196–202.
Mott, N. F. (1968). *Rev. Mod. Phys.* **40**, 677–683.
Newton, M. A. (2009). *Top. Catal.* **52**, 1410–1424.
Newton, M. A., Chapman, K. W., Thompsett, D. & Chupas, P. J. (2012*a*). *J. Am. Chem. Soc.* **134**, 5036–5039.
Newton, M. A., Di Michiel, M., Kubacka, A. & Fernández-García, M. (2010). *J. Am. Chem. Soc.* **132**, 4540–4541.
Newton, M. A., Jyoti, B., Dent, A. J., Fiddy, S. G. & Evans, J. (2004). *Chem. Commun.* pp. 2382–2383.
Newton, M. A., Michiel, M. D., Kubacka, A., Juez, A. I. & García, M. F. (2012*b*). *Angew. Intl. Ed.* **51**, 2363–2367.
Newton, M. A., Nijhatten, P. van & Kansiz, M. (2012*c*). In preparation.
Newton, M. A. & van Beek, W. (2010). *Chem. Soc. Rev.* **39**, 4845–4863.
Orlov, Y. I. (2002). *Glass Phys. Chem.* **28**, 281–287.
Palczewski, K., Kumasaka, T., Hori, T., Behnke, C. A., Motoshima, H., Fox, B. A., Le Trong, I., Teller, D. C., Okada, T., Stenkamp, R. E., Yamamoto, M. & Miyano, M. (2000). *Science*, **289**, 739–745.
Park, J. H., Scheerer, P., Hofmann, K. P., Choe, H. W. & Ernst, O. P. (2008). *Nature (London)*, **454**, 183–187.
Peierls, R. E. (1955). *Quantum Theory of Solids.* Clarendon: Oxford University Press.
Petkov, V. (2008). *Mater. Today*, **11**, 28–38.
Powell, B. J. & McKenzie, R. H. (2006). *J. Phys. Condens. Matter*, **18**, R827–R866.
Qazilbash, M. M., Brehm, M., Chae, B. G., Ho, P. C., Andreev, G. O., Kim, B. J., Yun, S. J., Balatsky, A. V., Maple, M. B., Keilmann, F., Kim, H. T. & Basov, D. N. (2007). *Science*, **318**, 1750–1753.
Radu, I., Schleeger, M., Bolwien, C. & Heberle, J. (2009). *Photochem. Photobiol. Sci.* **8**, 1517–1528.
Rau, J. V., Generosi, A., Komlev, V. S., Fosca, M., Fomin, A. S., Barinov, S. M. & Rossi Albertini, V. (2010). *Dalton Trans.* **39**, 11412–11423.
Rödig, C., Chizhov, I., Weidlich, O. & Siebert, F. (1999). *Biophys. J.* **76**, 2687–2701.
Schubert, M. M., Haring, T. P., Brath, G., Gasteiger, H. A. & Behm, R. J. (2001). *Appl. Spectrosc.* **55**, 1537–1543.
Sheregii, E. M., Cebulski, J., Marcelli, A. & Piccinini, M. (2009). *Phys. Rev. Lett.* **102**, 045504.
Siebert, F. (1995). *Isr. J. Chem.* **35**, 309–323.
Smirnov, V. V., Rau, J. V., Generosi, A., Rossi Albertini, V., Ferro, D. & Barinov, S. M. (2010). *J. Biomed. Mater. Res. B*, **93**, 74–83.
Suzuki, O., Nakamura, M., Miyasaka, Y., Kagayama, M. & Sakurai, M. (1991). *Tohoku J. Exp. Med.* **164**, 37–50.
Tanaka, Y., Uozaki, Y., Nozaki, K., Ito, K., Yamasaki, K., Terauchi, H., Takahashi, I., Tahara, K. & Ishikawa, T. (2011). *J. Phys. Conf. Ser.* **278**, 012018.
Tocchio, L. F., Parola, A., Gros, C. & Becca, F. (2009). *Phys. Rev. B*, **80**, 064419.
Yao, T., Zhang, X., Sun, Z., Liu, S., Huang, Y., Xie, Y., Wu, C., Yuan, X., Zhang, W., Wu, Z., Pan, G., Hu, F., Wu, L., Liu, Q. & Wei, S. (2010). *Phys. Rev. Lett.* **105**, 226405.
Zhao, H. Y., Nenoff, T. M., Jennings, G., Chupas, P. J. & Chapman, K. W. (2011). *J. Phys. Chem. Lett.* **2**, 2742–2746.